



UNIVERSITY OF LEEDS

This is a repository copy of *Modelling and simulation of counter-current and confined jet reactors for hydrothermal synthesis of nano-materials*.

White Rose Research Online URL for this paper:  
<http://eprints.whiterose.ac.uk/83208/>

Version: Accepted Version

---

**Article:**

Ma, CY, Chen, M and Wang, XZ (2014) Modelling and simulation of counter-current and confined jet reactors for hydrothermal synthesis of nano-materials. *Chemical Engineering Science*, 109. 26 - 37. ISSN 0009-2509

<https://doi.org/10.1016/j.ces.2014.01.006>

---

**Reuse**

Unless indicated otherwise, fulltext items are protected by copyright with all rights reserved. The copyright exception in section 29 of the Copyright, Designs and Patents Act 1988 allows the making of a single copy solely for the purpose of non-commercial research or private study within the limits of fair dealing. The publisher or other rights-holder may allow further reproduction and re-use of this version - refer to the White Rose Research Online record for this item. Where records identify the publisher as the copyright holder, users can verify any specific terms of use on the publisher's website.

**Takedown**

If you consider content in White Rose Research Online to be in breach of UK law, please notify us by emailing [eprints@whiterose.ac.uk](mailto:eprints@whiterose.ac.uk) including the URL of the record and the reason for the withdrawal request.



[eprints@whiterose.ac.uk](mailto:eprints@whiterose.ac.uk)  
<https://eprints.whiterose.ac.uk/>

# **Modelling and Simulation of Counter-Current and Confined Jet Reactors for Hydrothermal Synthesis of Nano-materials**

**Cai Y. Ma<sup>1</sup>, Man Chen<sup>1</sup>, Xue Z. Wang<sup>2,1\*</sup>**

<sup>1</sup>Institute of Particle Science and Engineering, School of Process, Environmental and Materials  
Engineering, University of Leeds, Leeds LS2 9JT, United Kingdom

<sup>2</sup>School of Chemistry and Chemical Engineering, South China University of Technology, Guangzhou  
510640, China

**\* Corresponding author:**

Prof Xue Z Wang

School of Chemistry and Chemical Engineering

South China University of Technology

Guangzhou 510640, China

Tel 0086 (0)20 8711 4000

Email: xuezhongwang@scut.edu.cn

## **Abstract**

A confined jet mixer and a counter-current mixer for the continuous hydrothermal flow synthesis of TiO<sub>2</sub> nano-materials under supercritical water conditions have been investigated using computational fluid dynamics (CFD). The fluid flow and heat transfer behaviour, including velocity and temperature profiles in both reactor configurations, are studied using the CFD tool ANSYS Fluent. The tracer concentration profiles are also simulated via solving species equations from which the mixing behaviour in the reactors is examined. A combined CFD and population balance model is used to predict the size distribution. The predicted temperature distributions for both reactors were found to be in good agreement with experimentally measured data. Detailed comparison of the hydrodynamic and thermal behaviour, and particle size distributions between the two reactors helped in the identification of key factors that affect the reactor performance, and also provided suggestions for reactor design optimisation and scale-up.

**Keywords:** Counter-Current Reactor, Confined Jet Mixer, Computational Fluid Dynamics, Supercritical Water, Mixing.

## Introduction

Hydrothermal synthesis processes, in particular those operated in continuous mode under supercritical water conditions, have been studied previously to produce metal oxide particles in nano-size range (1 – 100 nm typically) (Bermejo and Cocero, 2006; Moussiere et al., 2007; Adschiri et al., 2000; Adschiri et al., 1992; Cabanas and Poliakoff, 2001; Ohara et al., 2004; Otsu and Oshima, 2005; Aimable et al., 2009). Continuous hydrothermal processes have a wide range of applications including: the synthesis of catalysts and photo-catalysts, electronic materials, bio-medical materials, fuel cell materials, thin films, inks, disinfectants, amongst others (Lester et al., 2006). The continuous hydrothermal flow synthesis (CHFS) process is relatively green as it uses water as a major reagent rather than organic solvents. Early hydrothermal synthesis processes were based upon batch reactors, whilst more recently the continuous hydrothermal process has been developed to a commercial scale set-up in Korea (Adschiri et al., 2011). The CHFS method has shown many advantages over batch mode operation (Adschiri et al., 1992) including finer control over the reaction conditions, which often leads to a reduction of batch to batch variation (Boldrin et al., 2006; Chaudhry et al., 2006; Darr and Poliakoff, 1999). In a CHFS process, reactions between supercritical water and solutions of metal salts take place in an in-pipe mixer on a rapidly decreasing time scale (e.g. a few milliseconds). Understanding the mixing, temperature and velocity profiles in the reactor is clearly critical to reactor design and optimisation, as well as for the development of a successful scale-up strategy. It is often difficult and costly to achieve these goals iteratively through experimentally testing various design alternatives (Tighe et al., 2012). The purpose of this study was to apply modelling techniques of computational fluid dynamics (CFD) to support the reactor design, optimisation and scale-up of the CHFS process.

CFD modelling of standard stirred tank reactors for processing of particles, such as for crystallisation (Li et al., 2004) and for gas liquid mixing (Zhang et al., 2009) have been widely studied. However, research work on CFD modelling for hydrothermal synthesis, especially using impinging jet reactors operating under supercritical water conditions is still limited and is reviewed

below. Woo et al. (Woo et al., 2009) studied the use of combined CFD and population balance equations for modelling anti-solvent crystallisation of ovastatin and polymorphic crystallisation of L-histidine in continuous confined impinging jet mixers under atmospheric pressure. Moussiere et al. (Moussiere et al., 2007) reported CFD simulation of impinging jet reactors for the oxidation of organic matter as a means of waste remediation. Lester et al. (Lester et al., 2006) used CFD to simulate the velocity distributions inside a counter-current nozzle reactor. However, in the simulation, methanol and sucrose at ambient temperature and pressure were used to model supercritical water and metal salt solution at critical water condition. In the work, the steady-state concentration distribution of methylene blue dye from experiment and its equivalent CFD simulation presented by velocity distribution were compared. Aimable et al. (Aimable et al., 2009) simulated the mixing zone of a reactor with X-shaped geometry to predict the distributions of temperature and velocity, but the simulation was not validated experimentally. Kawasaki et al. (Kawasaki et al., 2010) studied a T-shaped mixer for continuous supercritical hydrothermal synthesis of TiO<sub>2</sub> nano-particles. CFD simulations were performed to obtain velocity and temperature profiles under different operating conditions, but the results were not validated with experimental data. Pure water properties were used in the simulations due to the low Ni(NO<sub>3</sub>)<sub>2</sub> molality. Sierra-Pallares et al. (Sierra-Pallares et al., 2011; Sierra-Pallares et al., 2009) attempted to quantify the mixing efficiency in turbulent supercritical water hydrothermal reactors including a T-shaped mixer and a counter-current reactor using the Reynolds averaged Navier Stokes approach coupled with an equation of state and a micromixing model. The mixing behaviour of both a T-shaped mixer and a counter-current reactor were compared to each other. However, the simulated velocity and dye concentration in the counter-current reactor were compared only with the experimentally obtained contours from the literature (Lester et al., 2006). The models were assessed using CFD in a submerged nitrogen jet and a supercritical carbon dioxide reactor. Demoisson et al. (Demoisson et al., 2011) also simulated the velocity and temperature distributions in a counter-current reactor operating under supercritical water conditions for nano-material formation using a CFD modelling method. A thermocouple was placed close to the reaction

zone and the measured temperature at this point was compared with the simulated value. Baldyga et al. (Baldyga et al., 2010; Baldyga et al., 2010) simulated anti-solvent precipitation processes for the generation of paracetamol and nicotinic acid from ethanol solution using supercritical carbon dioxide as an anti-solvent. The modelling method coupled momentum, species and energy balance with the population balance model to obtain profiles of flow, mixing, temperature and crystal size distribution. The simulated distributions of velocity, temperature and species concentration did not compare with the experimental data (which may be not available due to extremely difficult measurement conditions). In summary, the previous work reviewed above is valuable and inspiring, but the majority of the published materials have not been able to compare simulation results with experimental data due to the difficulty of taking measurements at the high operating temperatures and pressures of hydrothermal processes. As such, some of the simulations reviewed above were not carried out under supercritical conditions (Woo et al., 2006), and were compared to ambient temperature analogues (Lester et al., 2006). The dramatic changes of water thermodynamic properties around the supercritical point posed great challenges to the modelling of fluid flow, heat transfer, nanoparticle formation and particle growth processes in hydrothermal reactors under supercritical conditions. Furthermore, only a few papers dealt with nano-particle formation. Finally, little has been done on comparing the performance of different reactor configurations and designs.

In this paper, CFD models were developed using ANSYS Fluent (2010) and applied to a counter-current reactor and a confined jet mixer in a CHFS system for the synthesis of nanomaterials. The purpose was to investigate and develop understanding of the hydrodynamic, heat transfer and mixing behaviour of different reactor configurations. Such knowledge is needed for optimum design of a reactor and for successful scale-up. Experiments were also carried out under similar operating conditions for both reactors to collect experimental data for the validation of simulation results. The study has focused on the investigation of the effect of reactor configurations on the process behaviour such as velocity, temperature and concentration distributions. The governing equations for mass, momentum, species concentration and turbulence, together with the supercritical water properties used

in this study are described in Section 2. Section 3 describes the processes of mixing in a counter-current reactor and a confined jet mixer and also presents the experimental procedure of obtaining temperature profiles from reactors operating at temperatures and pressures used for the synthesis of nanoparticles. The computational details and solution methods are introduced in Section 4. Simulated results are analysed and discussed in Section 5, which is followed by concluding remarks in the final section.

## Mathematical formulation

### Hydrodynamic and mixing models

Based on time-averaged quantities obtained from Reynolds average of the instantaneous equations which are derived from the conservation laws of mass, momentum and energy, the three-dimensional continuity, momentum and enthalpy equations were numerically solved to obtain hydrodynamic and thermal profiles. There exist several turbulence models including zero-/one-equation, two-equation ( $k - \varepsilon$ ,  $k - \omega$ , and the variations), and Reynolds stress models, of which the most commonly used one is the  $k - \varepsilon$  two-equation model. It is a semi-empirical model with robustness and reasonable accuracy for a wide range of turbulent flows. The turbulent kinetic energy  $k$  and its dissipation rate  $\varepsilon$  are the selected two quantities for which two additional transport equations are solved with standard empirical constants (Launder et al., 1975) :  $C_{1\varepsilon} = 1.44$ ,  $C_{2\varepsilon} = 1.92$ ,  $C_\mu = 0.09$ ,  $\sigma_k = 1.0$ ,  $\sigma_\varepsilon = 1.3$ .

Simulation of mixing was carried out by introducing a secondary liquid (with the same properties as the primary liquid) as an inert tracer into the primary liquid in the reactor. The temporal and spatial distributions of the tracer concentration were obtained from the solution of the Reynolds-averaged species transport equation below:

$$\frac{\partial \rho Y_i}{\partial t} + \frac{\partial \rho u_j Y_i}{\partial x_j} = \frac{\partial}{\partial x_i} \left( \Gamma_{i,\text{eff}} \frac{\partial Y_i}{\partial x_j} \right) \quad (1)$$

where the effective diffusion coefficient of species  $i$  is  $\Gamma_{i,\text{eff}} = \Gamma_i + \mu_t / \text{Sc}_t$ ,  $\rho$  is the mixture density,  $u_j$  is the mixture velocity,  $Y_i$  represents the species mass fraction,  $\Gamma_i$  the species diffusion coefficient,  $\mu_t$  the turbulent eddy viscosity, and  $\text{Sc}_t$  the turbulent Schmidt number.

### Thermodynamic properties

The IAPWS (International Association for the Properties of Water and Steam) formulation 1995 for the thermodynamic properties of ordinary water substance for general and scientific use was used to calculate the thermo-physical properties of water (Wagner and Pruß, 2002). However, since a large number of special functions were used in the formulation to fit a large amount of experimental data, it would be computationally costly to solve the formulated equations for each iteration and each mesh cell during CFD simulations. Considering the need for both efficiency and accuracy in this study, the water properties (Figure 1) were obtained from the National Institute of Standards and Technology (2009) using the 1995 IAPWS formulation (Wagner and Pruß, 2002), and were piece-wise curve-fitted in polynomial forms over several temperature ranges at a fixed pressure of 24.1 MPa (Ma et al., 2011). An example function for thermal conductivity ( $\kappa$ ) within a temperature range of 273 – 618K is given below:

$$\kappa = -0.267 + 4.61 \times 10^{-6} T - 5.48 \times 10^{-6} T^2 \quad (2)$$

The obtained functions were used to calculate thermodynamic properties in the simulations. For diffusion coefficients in the mixing study, the correlation from Liu and Macedo (Liu and Macedo, 1995) was used to estimate the water diffusivity ( $D_w$ ):

$$D_w = 1.8 \times 10^3 A \rho^{-1} + 10^{-4} B (\log \rho - 7.26) + 10^{-4} C + 2.37 \times 10^{-7} E \rho^{0.361} \quad (3)$$

with  $A = 7.59 \times 10^{-7} T^{0.455}$ ,  $B = 1.43 \times 10^{-3} + 0.223 T^1 - 2.43 \times 10^{-5} T$ ;  $C = 8.56 \times 10^{-2} + 8.6 T^1 - 1.28 \times 10^{-4} T$ ;  $E = -1.82 \times 10^{-2} + 2.92 \times 10^{-3} T - 8.35 \times 10^{-6} T^2$ .

### Experimental studies of a counter-current reactor and a confined jet mixer

The flow diagram of a counter-current reactor system and a confined jet mixer system used for temperature profiling and also nano-particle production experiments are shown in Figure 2. Deionised

water was pumped through a heated, helical coil using pump P1 at a fixed pressure of 24.1 MPa and a constant flowrate of 20 mL/min. Since water density, hence volumetric flowrate, varies with temperature, for comparison purposes in this study all volumetric flowrates were based on the density of water at atmospheric pressure and a temperature of 20°C. An electrical heater was used to heat the deionised water to a required temperature of 400°C. An aqueous precursor and an aqueous base were pumped using Pumps P2 and P3, respectively, at 24.1 MPa with a fixed flowrate of 10 mL/min from each pump. The fluids from P2 and P3 were then mixed before entering a counter-current reactor where the mixture stream from P2 and P3 is mixed with the stream from P1, to react and generate nanoparticles. For a confined jet mixer, the fluids from P2 and P3 were mixed thoroughly and the resulting mixture was then split equally into two streams before entering the mixer through the two inlets. The streams from the two inlets mixed with the stream from P1 and reacted, generating nanoparticles. The slurry containing nanoparticles then travelled upwards and left the reactor to enter a heat exchanger for rapid cooling before being collected as the product. In order to concentrate the study on fluid flow and heat transfer, the mixture stream from P2 and P3 (Figure 2) was mimicked using deionised water during temperature profiling experiments and CFD modelling with the same approach being employed in the literature (Kawasaki et al., 2010) for the CFD simulations of continuous supercritical hydrothermal synthesis of NiO nanoparticles, though studies are being carried out to combine CFD with population balance (PB) modelling for the prediction of flow field, heat transfer phenomenon and particle size distribution. Typical solid concentration in the nanoparticle slurry under the current operating conditions is ~ 0.1 % w/w, indicating that the product slurry is very dilute. Furthermore, typical nano-particle size is < 100nm. Therefore, it is reasonable to ignore the effect of nanoparticles on flow patterns in this study. The possible impact of existence of nanoparticle on heat transfer behaviour is something new, and no models available yet to be included in calculation. The current opinion seems being that nanoparticle might enhance heat transfer efficiency at steady state but in a dynamic environment such as the current scenario, its impact is almost negligible. As a result, and also due to the fact that only dilute slurry is produced during synthesis, it

is reasonable to suggest that the effect of nanoparticles on the magnitude of heat transfer will be minimal. Therefore the simulations carried out in the present study involved single phase flow with two components (water and supercritical water).

The detailed schematic diagram of a counter-current reactor used in the CHFS system (Figure 2) is illustrated in Figure 3(a). The counter-current reactor consists of an inner tube ( $D_i = 1.75$  mm in diameter) inserted into a larger outer tube. The superheated water flows through the inner tube to the mixing point to mix with the metal salt solution (Figure 3(a)). The generated product stream leaves the reactor to enter a tubular heat exchanger. Seven long, fine J-type thermocouples were inserted into the counter-current reactor at different locations along the z direction as shown in Figure 3(a). The tips of the thermocouples were floated in the bulk flow for the purpose of measuring bulk temperatures and also the difficulty in fixing them onto a wall. Therefore, the tips of the thermocouples were estimated to be positioned within 2 mm across the tube cross-section (x-y plane).

Figure 4(a) illustrates the detailed schematic diagram of a confined jet mixer used in the CHFS system (Figure 2). The confined jet mixer consists of an inner tube ( $D_i = 0.99$  mm in diameter) inserted upwards into a larger outer tube. The superheated water flows upwards in the inner tube to the mixing point to mix with the metal salt solution also flowing upwards from the two precursor streams (Figure 4(a)). The generated product stream then flows upwards to leave the mixer and enters a tubular heat exchanger. Ten long, fine J-type thermocouples were inserted into the confined jet mixer at different locations along the z direction as shown in Figure 4(a). Again the tips of the thermocouples were left unattached in the bulk flow with the positions of the tip of the thermocouples being estimated to within 2 mm across the tube cross-section (x-y plane).

### **Simulation of a counter-current reactor and a confined jet mixer**

#### Computational details

Figure 3(b) shows the computational domain of a counter-current reactor which includes a stainless steel inner tube for introducing supercritical water to the mixing point, an outer tube with precursor stream flowing upwards, an annular channel formed between the outer tube and the inner tube for

mixture/product stream to flow upwards, and an exit arm. The three-dimensional domain was discretised using GAMBIT software with  $6.26 \times 10^5$  cells. Figure 4(b) shows the computational domain of a confined jet mixer which includes a stainless steel inner tube for introducing supercritical water to the mixing point, an outer tube with precursor stream being introduced radially via two inlet arms and flowing upwards in the annular channel between the inner and outer tubes. The three-dimensional domain was discretised using GAMBIT software with  $2.96 \times 10^5$  cells.

The operating conditions used for the computational studies were taken directly from the experiments and listed in Table 1. The operating pressure for both streams was 24.1 MPa. The inlet temperature of the precursor stream was fixed at 20°C. For the study of mixing, a tracer with the same operating temperature, pressure and properties as the supercritical water was introduced into the supercritical water stream. The flowrates of the tracer and supercritical water streams were 1% and 99% respectively, of the total flowrate of supercritical water used, i.e. 0.2 and 19.8 mL/min.

Independence tests for mesh size and convergence tolerance were carried out to eliminate their effect on simulated results. The flow field and mixing in both reactors were simulated with three mesh sizes:  $4.1 \times 10^5$ ,  $6.26 \times 10^5$  and  $7.5 \times 10^5$  for the counter-current reactor, and  $1.4 \times 10^5$ ,  $2.96 \times 10^5$  and  $3.7 \times 10^5$  for the confined jet mixer. The simulated temperature values along  $y = 1.0$  mm with mesh sizes of  $2.96 \times 10^5$  and  $3.7 \times 10^5$  in the confined jet mixer are almost identical, while the temperature distribution near the exit of the supercritical water for a mesh size of  $1.4 \times 10^5$  shows much lower values. Similar results are observed for other flow properties. For the counter-current reactor, predicted flow properties with mesh size of  $4.1 \times 10^5$  have noticeable differences from those with mesh sizes of  $6.26 \times 10^5$  and  $7.5 \times 10^5$ . The mean residence times in both reactors with different mesh sizes were obtained from the tracer mass concentrations. For the counter-current reactor, the mean residence times at the outlet are 5.88s, 5.41s and 5.35s for mesh sizes of  $4.1 \times 10^5$ ,  $6.26 \times 10^5$  and  $7.5 \times 10^5$ , respectively. For the confined jet mixer, the mean residence times at the outlet are 1.3 s, 0.92 s and 0.9 s for mesh sizes of  $1.4 \times 10^5$ ,  $2.96 \times 10^5$  and  $3.7 \times 10^5$ , respectively. Therefore, the simulated results with the mesh sizes of  $6.26 \times 10^5$  for the counter-current reactor and

$2.96 \times 10^5$  for the confined jet mixer are selected as mesh-independent in terms of both flow field and mixing.

#### Solution method

The mass, momentum and energy conservation equations and species transport equation, together with the equations for turbulent quantities,  $k$  and  $\varepsilon$ , were solved using ANSYS Fluent software (2010) to obtain the velocity, temperature and species distributions in the counter-current reactor and confined jet mixer. The species equations were solved with the steady-state flow and temperature profiles obtained as the initial values. Standard  $k$ - $\varepsilon$  model equations with standard wall functions (Launder and Spalding, 1974) were used. Standard SIMPLE pressure-velocity coupling was used with a second order upwind scheme being employed for the discretisation of the convection terms in the governing equations. It is known that the first order upwind scheme can introduce severe numerical diffusion in the solution, the second order upwind scheme produces less numerical diffusion, hence higher accuracy, and central difference scheme will produce numerical dispersion including undershoots and overshoots with a discontinuity. Other high order discretisation schemes can further improve the accuracy but require more CPU time. Therefore in this study involving three-dimensional flow, heat transfer and mixing etc., the second order upwind scheme was selected. Due to the insulation of the system, heat losses through the outer wall of the reactor were assumed to be negligible, i.e. an adiabatic boundary condition. The mass inlet flow mode was used to calculate the inlet velocities of both supercritical water and precursor streams. Constant inlet temperatures for the inlet fluids were specified. A typical turbulent intensity of 10% and the corresponding hydrodynamic diameters were used for the inlet conditions for turbulence with a value of 5% for the inlet turbulent intensity being tested and producing very similar simulation results. The outlet flow mode was used for their corresponding exit boundaries, which specify fully developed outlet flow conditions. Standard non-slip wall boundary conditions were applied in the studies with the standard turbulent wall function (Launder and Spalding, 1974) being used.

## Results and discussion

### Fluid flow and heat transfer study

Figure 5 shows the velocity vectors, contours of temperature and density distributions around the supercritical exit region of the counter-current reactor and confined jet mixer. The counter-current reactor (Figure 3(a)) has an inlet supercritical water temperature of 400°C with a flowrate of 20 mL/min, and an inlet precursor temperature of 20°C with a flowrate of 20 mL/min. Similar operating conditions are used for the confined jet mixer with the inlet precursor flowrate of 20 mL/min being equally split into two streams (Figure 4(a)). For the counter-current reactor, the supercritical water stream penetrated into the up-coming precursor stream to form a recirculation zone surrounding the supercritical water jet (Figure 5(a1)), which enhanced the mixing between the supercritical water and precursor streams. The mixture then went through the annular section to the product exit. Note that for comparison purposes, Figure 5(a1, b1) were plotted with a rotation of 180°. For the confined jet mixer, the supercritical water stream flows upwards from the inner pipe with the precursor stream flowing in the same direction but in an annulus surrounding the inner pipe. At the exit of the supercritical water stream, the two streams form a confined co-current flow configuration, in which the supercritical water jet entrains the precursor stream and forms a recirculation zone surrounding the jet (Figure 5(a2)). The penetration distances for the counter-current reactor and the confined jet mixer are about 5.7 and 13.4 times of their jet exit diameters, respectively. The pure precursor stream in the counter-current reactor can only meet the incoming supercritical water stream which may have mixed with the precursor and product due to the entrainment in the recirculation zone (Figure 5(a1)). As shown in Figure 5(a2), the pure precursor stream in the confined jet mixer is strongly entrained into the supercritical water stream at the jet exit as a result of the high momentum from the supercritical water jet. Because the tube length is shorter and tube diameter is smaller for the supercritical water stream, the total amount of heat transfer from the supercritical water in the tube to the precursor flow in the annular section is much smaller for the confined jet reactor. Since as modelled that the temperature at the tube exit point was still higher than the critical temperature of water, the water

ejected from the tube exit was still in supercritical condition. On the contrary, as modelled, the water stream at the tube exit for the counter-current reactor was already in sub-critical state. Therefore it is not surprising that as shown in (Figure 5(b2)), the temperature distribution for the confined jet mixer quickly reaches their final outlet values about 2 mm from the jet exit ( $z = 0$ ) in most regions, and the length of the temperature core is shorter than that for the counter-current reactor (Figure 5(b1)).

Figure 6 shows the variations of axial velocity, temperature and tracer concentration along the central line ( $x = 0, y = 0$ ) of both reactors and also the temperature and tracer concentration distributions along a line of ( $x = 0, y = 1.7$  mm) for the counter-current reactor and of ( $x = 0, y = 1$  mm) for the confined jet mixer in the  $z$  direction. The axial velocity, temperature and tracer concentration distributions were normalised by their corresponding inlet values, i.e. inlet axial velocity, temperature and tracer concentration (mass fraction) of 0.94 m/s, 400°C and 0.01, respectively, for the counter-current reactor, and 3.08 m/s, 400°C and 0.01 for the confined jet reactor. It can be seen from Figure 6 that from the supercritical water inlet to the exit, the supercritical water stream cooled down from 400°C to sub-critical conditions in the counter-current reactor, which resulted in a sub-critical stream temperature at the jet exit, hence much lower axial velocity (about 41% of the inlet axial velocity). This led to slow mixing between the supercritical water and the precursor streams, hence a longer distance for the decay of tracer mass, which may affect nanoparticle product quality. However, for the confined jet mixer, the supercritical water stream is still under supercritical conditions with a temperature of 388°C when it exited from the inner pipe, hence producing an exit axial velocity of 2.2 m/s (about 71% of the corresponding inlet axial velocity). Therefore, the confined jet mixer has a considerably shorter mixing distance than the counter-current reactor due to the enhanced mixing. For the counter-current reactor, the temperature profile in the  $z$  direction, along a line (1.7 mm) away from the reactor centre, shows a temperature jump from the upcoming precursor stream (due to spreading of the high temperature water jet), then a temperature dip caused by the recirculation of the mixture of high temperature water, tracer and precursor streams. The product stream entering the annular section is also subject to heating from the supercritical water

in the inner tube. The recirculation brought back the mixture with higher tracer concentration, hence in the temperature dipping region, a tracer concentration jump occurs before the tracer reaches a well-mixed level (0.005) in the annular section. For the confined jet mixer, the temperature along a line 1.0 mm away from the mixer centre jumped to the outlet temperature a short distance above the exit of the inner tube (after the precursor stream was ejected from the annular section). Figure 5(a2) shows a strong recirculation surrounding the supercritical water jet, hence the enhanced mixing. However, the small increase of tracer concentration after the precursor exit indicated that the strong recirculation brought back some of the mixture. The counter-current reactor has an inner tube diameter of 1.75 mm which is about 1.8 times of the inner tube diameter for the confined jet mixer. Therefore, the smaller inner tube diameter and the supercritical exit temperature led to an axial velocity at the exit of the inner tube being  $\sim 5.6$  times of that in the counter-current reactor. The mixing distances, defined as the tracer core length along the reactor centreline from the supercritical water exit to a centreline point with a tracer concentration of 0.05 in mass fraction (fully mixing level at the reactor outlet), are estimated to be 8.5 and 5.0 times of the jet exit diameters respectively, for the counter-current and confined jet reactors, which confirms significantly faster mixing for the confined jet mixer.

The predicted and measured temperatures along the  $z$  direction were compared in Figure 7. As the locations of the thermocouple tips can vary within 2 mm on the  $x$ - $y$  plane in the annular section, i.e.  $y = 1.6 - 3.5$  mm for the counter-current reactor and  $y = 1.0 - 2.0$  mm for the confined jet mixer, the predicted results at  $y = 1.7$  and 2.9 mm for the counter-current reactor, and  $y = 1.0$  and 1.2 mm for the confined jet mixer were plotted in Figure 7 (a) and (b), respectively. It can be seen that the predicted results are in good agreement with the measurements. The outlet temperatures of the reactors can be calculated from an overall heat balance (Tighe et al., 2012), which are shown as a thick solid line in Figure 6(a) and a dashed line in Figure 6(b). The simulated outlet temperatures are 304.8 and 305.3°C for the counter-current reactor and confined jet mixer respectively, which are very close to the theoretical value of 307°C.

### **Study on mixing behaviour**

Contours of tracer concentrations in mass fraction near the exit region of the supercritical water jet at different instants after starting the transient simulations in both reactors are plotted in Figure 8. For the counter-current reactor, Figure 8(a1 – a8) illustrated the tracer concentration contours at twelve time instants. It can be seen that the tracer slowly ejects from the inner tube exit into the region to meet the coming precursor stream. Note that for comparison purposes, Figures 8(a1 – a8) were plotted with a rotation of  $180^\circ$ . At a time instant of 9 s (Figure 8(a7)), the tracer distributions are very close to those at time instant of 15 s (Figure 8(a8)). Therefore the overall mixing time for this reactor configuration is 9 s under the current operating conditions. For the confined jet mixer, the tracer concentration contours at eight time instants are shown in Figure 8(b1 – b8). The tracer concentration distributions reach the steady-state after only 3 s from the start of the transient simulation as shown in Figure 8(b1 – b6). This may be attributed to a higher exit temperature and a higher exit velocity at the inner tube exit for the confined jet mixer, and also the direct entrainment of the precursor stream into the supercritical water stream (Figure 5(a2)), hence the tracer stream quickly mixing with the entrained precursor stream. Therefore, the confined jet mixer under the current operating conditions provides much faster mixing than the counter-current reactor.

In Figure 8(a8, b8), the circle points are the monitoring locations along the central line of the reactors, where the tracer concentrations were recorded during the whole transient simulations. A normalised distance for a monitoring point,  $\Delta L/D_i$ , is defined as the distance between the monitoring point and the supercritical water jet exit in the centreline of the reactor,  $\Delta L$ , divided by the inner tube diameter of the supercritical water,  $D_i$  ( $D_i = 1.75$  mm for the counter-current reactor and 0.99 mm for the confined jet mixer). The variations of tracer mass fraction at the four monitoring points, A1 ( $\Delta L/D_i = 0$ ), A2 ( $\Delta L/D_i = 0.5$ ), A3 ( $\Delta L/D_i = 2$ ), A4 ( $\Delta L/D_i = 3$ ), for the counter-current reactor as shown in Figure 8(a12), and B1 ( $\Delta L/D_i = 0$ ), B2 ( $\Delta L/D_i = 0.5$ ), B3 ( $\Delta L/D_i = 2$ ), B4 ( $\Delta L/D_i = 8$ ), for the confined jet mixer as shown in Figure 8(b8), during the time period of 15 s are recorded during the mixing simulations. The monitored tracer mass fraction distributions at each monitoring point were normalized by the corresponding fully mixed mass fraction,  $c_\infty$ . The local mixing times, defined as

the time required for the local tracer mass fraction to reach 99% of  $c_\infty$ , for the four monitoring points of A1 – A4 ( $\Delta L/D_i = 0, 0.5, 2$  and  $3$ ) were estimated from the predicted tracer mass fractions with the values of 1.1, 2.5, 3.5 and 5.8 s, respectively, for the counter-current reactor. For the confined jet mixer, the local mixing times obtained from the four monitoring points of B1 – B4 ( $\Delta L/D_i = 0, 0.5, 2$  and  $8$ ) are 0.1, 0.6, 1.0 and 1.2 s, respectively. According to the definition of a local mixing time, slow mixing behaviour usually leads to longer local mixing time. By comparing the local mixing times at the monitoring points of A1 – A4 and B1 – B4, it was found that, with the same normalised distances for both reactors, the local mixing times for the counter-current reactor are over three times longer than those for the confined jet mixer. This finding is understandable since the high momentum of the supercritical water jet at point B1 of the confined jet mixer and its direct entrainment of fresh precursor fluid from the annular tube section into the jet accelerates. The fully mixed tracer concentration in mass fraction at the reactor outlet is 0.005 for both reactors under the current operating conditions.

The residence time distribution,  $E(t)$ , is defined as a probability distribution function which shows the amount of time for a fluid element flowing through a monitoring cell (such as A1 – A4, B1 – B4) or a whole reactor. The residence time distributions (solid lines) for the eight monitoring points and the outlet areas for both reactors were obtained by differentiating the tracer concentration profiles against time. The mean residence times obtained for the monitored points A1 – A4 and also outlet in the counter-current reactor are 0.74, 0.75, 0.78, 0.82 and 5.41 s, respectively, with the corresponding variances being 0.107, 0.111, 0.132, 0.169 and 1.883 s. The mean residence times for the five locations (B1 – B4 and outlet) in the confined jet mixer were calculated to be 0.044, 0.046, 0.05, 0.1 and 0.92 s, respectively, with the corresponding variances being 0.038, 0.039, 0.043, 0.169 and 0.485 s. It is clear that the mean residence times and the variances for the confined jet mixer are smaller than those for the counter-current reactor. Furthermore, the residence time distributions in the counter-current reactor, in particular points A2 – A4, have long tails before reaching their corresponding well-mixed levels. The tracer concentrations and the corresponding residence time

distributions at the product outlet for both reactors (as shown in Figure 9) demonstrated that the confined jet mixer can reach the final well-mixed level of 0.005 in mass fraction within 5 s which is much shorter than a time of over 30 s required for the counter-current reactor. The residence time distribution for the confined jet mixer has a much sharper distribution with a much smaller tail comparing to that for the counter-current reactor. This result indicates that the confined jet mixer has a much faster mixing behaviour under the current operating conditions. We attribute this to its strong entrainment of fresh precursor into the supercritical water stream which is caused by the higher exit temperature of the supercritical water, hence higher exit velocity (momentum).

The Reynolds number,  $Re$ , at the jet exit ( $z = 0$ ) is defined as the relative magnitude between the momentum of a supercritical water jet and the viscous drag force and the Froude number,  $Fr^2$ , at  $z = 0$  can be estimated by the relative magnitude of the momentum of the jet against the buoyancy force (Tighe et al., 2012). The numerically predicted  $Re$  and  $Fr^2$  at the jet exit ( $z = 0$ ) for the counter-current reactor are 4082 and 7.1, which are in reasonable agreement with the values of 3600 and 6.2 determined from experimental temperature profiles and supercritical water properties. For the confined jet mixer, the numerically predicted  $Re$  and  $Fr^2$  at  $z = 0$  are 13643 and 124.7, respectively, which are much higher than those from the counter-current reactor. As discussed in Section 5.1, the supercritical water stream at the inner tube exit ( $z = 0$ ) became sub-critical for the counter-current reactor because of the heavy heat losses from the supercritical water to the product slurry through the wall of the inner tube, while, on the contrary, the water jet at  $z = 0$  for the confined jet mixer was still in supercritical state. This, together with the fact that the inner tube diameter for the confined jet mixer is 1.8 times smaller than that for the counter-current reactor, led to a momentum-dominated supercritical water jet at  $z = 0$  for the confined jet mixer, hence much higher Reynolds and Froude numbers. The fact that the reactor flow characteristics in the jet exit region became more turbulent and less driven by buoyancy in the confined jet mixer helped it to generate greater recirculation around the jet and also faster mixing between the supercritical water and the precursor streams.

Parametric studies under various operating conditions including the inlet flowrate and temperature of supercritical water, and the inlet flowrate of precursor have been carried out. Detailed simulated results have been reported at a conference (Ma et al., 2012). The operating conditions used for comparison for the two reactors were selected based on these results. Below when the particle formation model is integrated with CFD simulation, more operating conditions will be studied for comparison of the two reactor configurations.

As the sizes of the counter-current and confined jet reactors are slightly different, it might be debatable to make comparison between the confined jet mixer and the counter-current reactor based on their current reactor sizes for each reactor configuration. As a result, a new counter-current reactor was designed by reference to the design and sizes of the confined jet reactor: for the supercritical water tube, the new counter-current reactor has exactly the same tube diameter, tube length and insertion length as the confined jet mixer. Simulation was performed for the new counter-current reactor under the same conditions as for the confined jet reactor. It was found that the temperature near the exit of the supercritical water was higher than that for the original counter-current reactor; this increased the exit velocity of the supercritical water, hence achieving improved mixing. However, the temperature bump near the exit of the supercritical water still existed (simulation results are not given here due to consideration of saving space) and the residence time was still about 2~3 times longer than the confined jet mixer. It was also found that the new counter-current reactor has a similar flow pattern as the original counter-current reactor, indicating that for the counter-current reactor configuration, the fact that the mixture of supercritical water and precursor enters the recirculation region is most likely the main contributor to the long residence time.

#### Particle size distributions

Population balance modelling (PBM) simulates particle size distribution (PSD) during processing of particles. It takes into account the complex behaviour of nucleation, growth and particle interactions such as breakage and aggregation. Combined CFD-PBM models have previously been applied to study liquid-solid systems such as crystallization. In this work, the phenomena of

nucleation, growth and aggregation of TiO<sub>2</sub> nanoparticles were included in the simulations using user-defined functions through the PBM add-on module in the ANSYS Fluent package (2010). The nucleation and growth models, chemical composition and solubility equations can be found in our previous publication (Chen et al., 2011). The free molecular model was used to study particle aggregation behaviour with the Brownian kernel function being selected as the aggregation kernel based on the theory that Brownian motion is the most important transport mechanism in suspensions containing nano- and sub-micron particles (Peukert et al., 2005; Testino et al., 2005).

The PBM equation was coupled with flow dynamics using the Sauter mean diameter approach and the homogeneous discrete method (Hounslow et al., 1988; Lister et al., 1995) was used to solve the balance equations. In order to study the effect of particle agglomeration on particle size distribution, simulations were carried out in two scenarios: 1) particle growth according to surface growth theory, 2) particle enlargement from surface growth and aggregation. For the pure surface growth model, particles were classified into ten size classes ranging from 1 to 512 nm, while for the aggregation modelling, the aggregate sizes were extended to 4 μm. The selection of the size ranges was based on reported experimental results (Chen et al., 2012; Alonso et al., 2007; Kawasaki et al., 2009; Hakuta et al., 2004; Hayashi and Torii, 2002) with aggregation being taken into account. The size distribution of the TiO<sub>2</sub> nanoparticles from both reactors was simulated. The particle sizes obtained from the models are reported as the Sauter mean diameter  $D_{3,2}$  (i.e. mean size based on surface area) and length mean diameter  $D_{1,0}$  (i.e. mean size based on particle diameter) at the reactor outlet surface as described by Equations 4 and 5:

$$D_{3,2} = \frac{1}{N} \times \frac{\sum_{i=1}^N NiDi^3}{\sum_{i=1}^N NiDi^2} \quad (4)$$

$$D_{1,0} = \frac{1}{N} \times \sum_{i=1}^N NiDi \quad (5)$$

where  $D$  is particle diameter (nm),  $N$  is total number of particles (#),  $Di$  is the particle diameter at the  $i$ th size class,  $Ni$  is the number of particles within the  $i$ th size class.

For the confined jet mixer, if only surface growth is considered, the particles predicted have a small length mean size of 3.47 nm and a narrow size distribution with the Full Width at Half Maximum (FWHM) being approximately 0.8 nm (Figure 10, solid line). The particle sizes appeared to be uniform on the outlet surface, with a small percentage of larger particles being formed near the inner wall surface of the reactor. In the case of including particle aggregation phenomenon into the prediction, a greater proportion of large size aggregates were formed, adding mass on/near the reactor boundary (Figure 10, dotted line). This is probably related to the size dependence of the Brownian aggregation kernel, as smaller particles are more likely to collide and produce an aggregate (Ginter and Loyalka, 1996; Smoluchowski, 1917). The predicted particle mean size of the counter-current reactor is approximately 5 times larger than that of the confined jet mixer as simulated in the growth model (Figure 10, dashed line). The result is consistent with the residence time difference between these two reactors that was highlighted earlier. In the counter-current reactor, the product slurry leaves the reactor outlet in the horizontal direction at low velocity. Gravity may affect large particles, hence they tend to stay near the bottom part of the outlet section, which potentially leads to the accumulation of big agglomerates in the area as predicted in the aggregation model (Figure 10, dotted and dashed line). The recirculation zone near the bottom of the outlet tube after a 90° bend may also contribute to the asymmetric mode of particle size distributions in the top and bottom direction. Also, the PSD produced in the counter-current reactor appears to be much wider than that of the confined jet mixer. This can be confirmed by the corresponding large difference between two reactors for both  $D_{3,2}$  and  $D_{1,0}$  which is usually due to a broad particle size distribution (Paul et al., 2003; Yang, 2003; Merkus, 2009). In general, as shown in Figure 10, the particles produced in the counter-current reactor are larger than those of the confined jet mixer and the predicted PSD also appeared to be wider. The difference may be related to the longer residence time in the counter current reactor.

### **Further discussions**

For the counter-current reactor, the water temperatures at the exit of the inner tube were much lower than the inlet temperatures of the supercritical water streams due to the huge heat losses through the

wall of the long inner tube into the annular section, hence their axial velocities being much lower than the inlet velocities of the supercritical water. This has been identified as one of the major factors affecting the reactor performance. Optimising the insertion length of the supercritical water pipe based on the existing reactor configuration is likely to improve the reactor performance. Furthermore, the much larger tube diameters used in the counter-current reactor also caused less effective mixing in the reactor compared to the performance in the confined jet mixer with smaller tube diameters. Therefore further studies will also be carried out to investigate the effect of pipe diameters to improve reactor performance. For the confined jet mixer, on the other hand, the positions of the supercritical water pipe, the pipe diameters used for the precursor and supercritical water streams, and different operating conditions will be studied in the future using simulation. During the manufacture and assembly of the reactors, the inner tube may not be placed exactly along the central line ( $x = 0, y = 0$ ) (Middelkoop et al., 2009), hence causing asymmetrical configuration and flow pattern. The effect of this geometrical asymmetry on the reactor performance also needs further work.

By comparing the reactor configurations of both counter-current and confined jet reactors, it is evident that the counter-current reactor mixing will affect its use for production of nano-materials as when they have been formed in the reactor, they will be subject to heating from the supercritical water in the inner tube when travelling up through the annular section to the outlet and also flowing through a  $90^\circ$  bend from the annular section to the outlet. This issue will increase the likelihood of CHFS-made nanomaterials further aggregation or growth and also potential deposition of materials on the wall during the  $90^\circ$  flow bending. However, for the confined jet mixer, the nanomaterial produced slurry flows upward to the outlet in a straight pipe and then enters a cooling system for fast cooling to quench any further processes (Ma et al., 2011). Therefore, the confined jet mixer configuration could offer advantages in the future as the technology is scaled-up.

### **Concluding remarks**

The fluid flow and heat transfer patterns, as well as the mixing behaviour in the counter-current and confined jet reactors for continuous hydrothermal flow synthesis of nanomaterials were investigated

using computational fluid dynamics models. The hydrodynamic and thermodynamic variables including velocity, temperature and mixing in both reactor configurations were simulated and compared. The predicted temperatures along the z direction in both reactors were found to be in good agreement with experimental data. The mixing study found that under the current reactor configurations and operating conditions, the mixing in the confined jet mixer is much faster than the counter-current reactor, and the residence time distribution for the counter-current reactor is broader with a long tail. The simulated size distributions of TiO<sub>2</sub> nanoparticles indicated that the faster mixing in the confined jet mixer produced more uniform size distribution. The study identified the major factors that affect the reactor performance with suggestions for reactor design optimisation and reactor scale-up. Future work is planned to extend the work to a pilot plant rig which has been built at University College London (Tighe et al., 2013; Gruar et al., 2013).

### **Acknowledgements**

Financial support from the UK Engineering and Physical Sciences Research Council (EPSRC) for the project: Continuous Hydrothermal Synthesis of Nanomaterials: From Laboratory to Pilot Plant (EP/E040624/1 for University of Leeds and EP/E040551/1 for University College London) is acknowledged. We would also like to thank the industrial collaborators including Johnson Matthey PLC, Resource Efficiency Knowledge Transfer Partnership, Sun Chemical, Neo Technologies, Malvern Instruments Ltd and Nanoforce Technology Ltd.

### **Notation**

A, B, C, E = terms used in diffusion coefficient calculation (Eq. 3)

$C_p$  = specific heat ( $\text{J kg}^{-1} \text{K}^{-1}$ )

$c$  = tracer mass concentration

$c_\infty$  = tracer mass concentration after fully mixed

$D$  = particle diameter (nm)

$D_w$  = water diffusivity ( $\text{m}^2 \text{s}^{-1}$ )

$D_i$  = diameter of an inner tube (m)

$E(t)$  = residence time distribution ( $s^{-1}$ )

$Fr^2$  = Frouder number

$g$  = gravity ( $m\ s^{-2}$ )

$k$  = turbulent kinetic energy ( $m^2\ s^{-2}$ )

$N$  = total number of particles (#)

$Re$  = Reynolds number

$Sc_t$  = turbulent Schmidt number

$T$  = temperature (K)

$T_{in}$  = inlet temperature (K)

$t$  = time (s)

$u$  = velocity ( $m\ s^{-1}$ )

$x, y, z$  = coordinate (m)

$Y_i$  = mass concentration of species  $i$

### **Greek Letters**

$\Delta L$  = distance between monitoring point and exit of supercritical water stream (m)

$\varepsilon$  = dissipation rate of  $k$  ( $m^2\ s^{-3}$ )

$D_i$  = molar diffusion coefficient of species  $i$  ( $m^2\ s^{-1}$ )

$D_{i,eff}$  = effective diffusion coefficient of species  $i$  ( $m^2\ s^{-1}$ )

$\kappa$  = thermal conductivity ( $W\ m^{-1}\ K^{-1}$ )

$\mu_t$  = turbulent eddy viscosity (Pa s);  $\rho$  = density ( $kg\ m^{-3}$ )

### **References**

2009. National Institute of Standard and Technology [www.nist.gov](http://www.nist.gov).

2010. ANSYS Fluent Package [www.fluent.co.uk](http://www.fluent.co.uk).

Adschiri, T., Hakuta, Y. and Arai, K., 2000. Hydrothermal synthesis of metal oxide fine particles at supercritical conditions. *Industrial and Engineering Chemistry Research*. 39, 4901-4907.

Adschiri, T., Kanazawa, K. and Arai, K., 1992. Rapid and continuous hydrothermal synthesis of boehmite particles in sub and supercritical water. *The Journal of the American Ceramic Society*. 75, 2615-2618.

Adschiri, T., Lee, Y.-W., Goto, M. and Takami, S., 2011. Green materials synthesis with supercritical water. *Green Chemistry*. 13, 1380-1390.

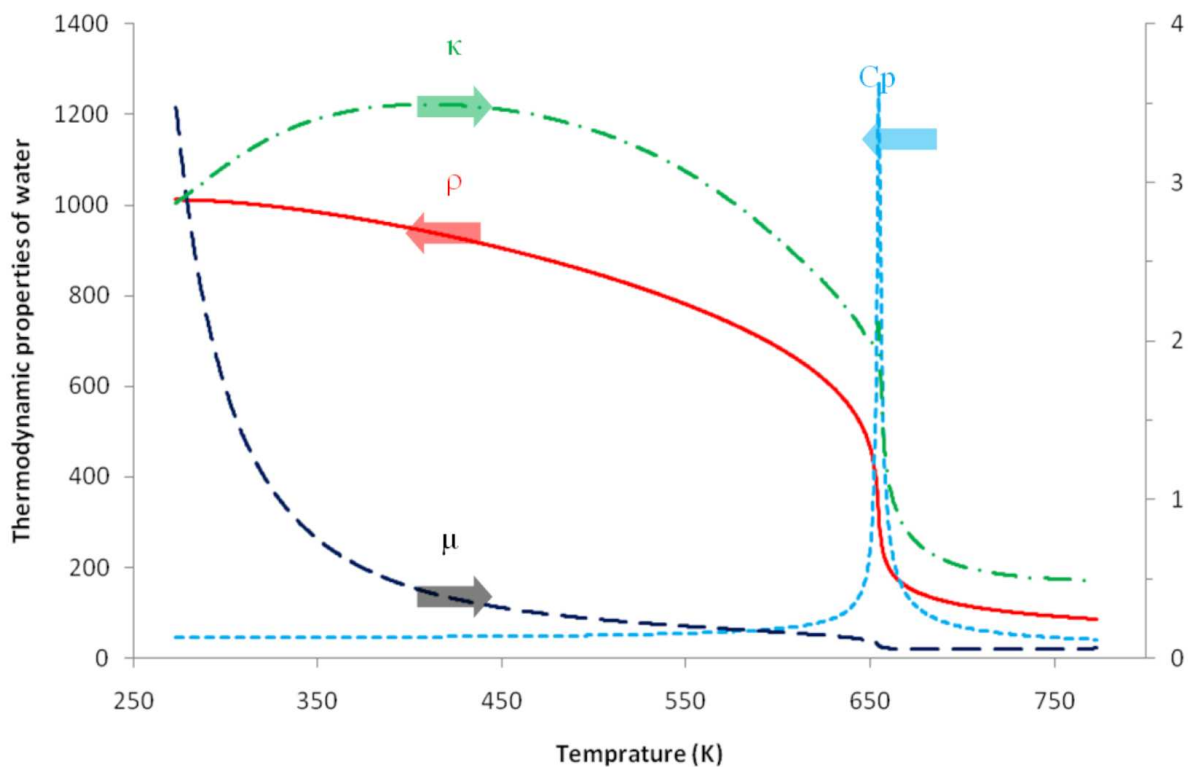
- Aimable, A., Muhr, H., Gentric, C., Bernard, F., Le Cras, F. and Aymes, D., 2009. Continuous hydrothermal synthesis of inorganic nanopowders in supercritical water: Towards a better control of the process. *Powder Technology*. 190, 99-106.
- Alonso, E., Montequi, I., Lucas, S. and Cocero, M.J., 2007. Synthesis of titanium oxide particles in supercritical CO<sub>2</sub>: Effect of operational variables in the characteristics of the final product. *The Journal of Supercritical Fluids*. 39, 453-461.
- Baldyga, J., Czarnocki, R., Shekunov, B.Y. and Smith, K.B., 2010. Particle formation in supercritical fluids - Scale-up problem. *Chemical Engineering Research and Design*. 88, 331-341.
- Baldyga, J., Kubicki, D., Shekunov, B.Y. and Smith, K.B., 2010. Mixing effects on particle formation in supercritical fluids. *Chemical Engineering Research and Design*. 88, 1131-1141.
- Bermejo, M.D. and Cocero, M.J., 2006. Supercritical Water Oxidation: A Technical Review. *AIChE Journal*. 52, 3933-3951.
- Boldrin, P., Hebb, A.K., Chaudhry, A.A., Otley, L., Thiebaut, B., Bishop, P. and Darr, J.A., 2006. Direct Synthesis of Nanosized NiCO<sub>2</sub>O<sub>4</sub> Spinel and Related Compounds via Continuous Hydrothermal Synthesis Methods. *Industrial and Engineering Chemistry Research*. 46, 4830-4838.
- Cabanas, A. and Poliakoff, M., 2001. The continuous hydrothermal synthesis of nanoparticulate ferrites in near critical and supercritical water. *Journal of Materials Chemistry*. 11, 1408-1416.
- Chaudhry, A.A., Haque, S., Kellici, S., Boldrin, P., Rehman, I., Fazal, A.K. and Darr, J.A., 2006. Instant nano-hydroxyapatite: A continuous and rapid hydrothermal synthesis. *Chemical Communications*. 21, 2286-2288.
- Chen, M., Ma, C.Y., Mahmud, T., Darr, J.A. and Wang, X.Z., 2011. Modelling and simulation of continuous hydrothermal flow synthesis process for nano-materials manufacture. *The Journal of Supercritical Fluids*. 59, 131-139.
- Chen, M., Ma, C.Y., Mahmud, T., Lin, T. and Wang, X.Z. 2012. Population Balance Modelling and Experimental Validation for Synthesis of TiO<sub>2</sub> Nanoparticles using Continuous Hydrothermal Process. In: Jin, Z.X., Xie, Z. and Gai, G.S., eds. *Measurement and Control of Granular Materials*. 508 vol.Section. 175-179.
- Darr, J.A. and Poliakoff, M., 1999. New Directions in Inorganic and Metal-Organic. Co-ordination Chemistry in Supercritical Fluids. *Chemical Reviews*. 99, 495-541.
- Demoisson, F., Ariane, M., Leybros, A., Muhr, H. and Bernard, F., 2011. Design of a reactor operating in supercritical water conditions using CFD simulations. Examples of synthesized nanomaterials. *Journal of Supercritical Fluids*. in press.
- Ginter, D.M. and Loyalka, S.K., 1996. Apparent size-dependent growth in aggregating crystallizers. *Chemical Engineering Science*. 51, 3685-3695.
- Gruar, R.I., Tighe, C.J. and Darr, J.A., 2013. Scaled-up a confined jet reactor for the continuous hydrothermal manufacture of nanoparticles. *Industrial and Engineering Chemistry Research*. (in press).
- Hakuta, Y., Hayashi, H. and Arai, K., 2004. Hydrothermal synthesis of photocatalyst potassium hexatitanate nanowires under supercritical conditions. *Journal of Materials Science*. 39, 4977-4980.
- Hayashi, H. and Torii, K., 2002. Hydrothermal synthesis of titania photocatalyst under subcritical and supercritical water conditions. *Journal of Materials Chemistry*. 12, 3671-3676.

- Hounslow, M.J., Ryall, R.L. and Marshall, V.R., 1988. A discretized population balance for nucleation, growth, and aggregation. *AIChE Journal*. 34, 1821-1832.
- Kawasaki, S.-i., Xiuyi, Y., Sue, K., Hakuta, Y., Suzuki, A. and Arai, K., 2009. Continuous supercritical hydrothermal synthesis of controlled size and highly crystalline anatase TiO<sub>2</sub> nanoparticles. *The Journal of Supercritical Fluids*. 50, 276-282.
- Kawasaki, S.I., Sue, K., Ookawara, R., Wakashima, Y., Suzuki, A., Hakuta, Y. and Arai, K., 2010. Engineering study of continuous supercritical hydrothermal method using a T-shaped mixer: Experimental synthesis of NiO nanoparticles and CFD simulation. *Journal of Supercritical Fluids*. 54, 96-102.
- Lauder, B.E., Reece, G.J. and Rodi, W., 1975. Progress in the development of a Reynolds-stress turbulence closure. *Journal of Fluid Mechanics*. 68, 537-566.
- Lauder, B.E. and Spalding, D.B., 1974. The numerical computation of turbulent flows. *Computer Methods in Applied Mechanics and Engineering*. 3, 269-289.
- Lester, E., Blood, P., Denyer, J., Giddings, D., Azzopardi, B. and Poliakoff, M., 2006. Reaction engineering: The supercritical water hydrothermal synthesis of nano-particles. *Journal of Supercritical Fluids*. 37, 209-214.
- Li, M., White, G., Wilkinson, D. and Roberts, K.J., 2004. LDA measurements and CFD modelling of a stirred vessel with a retreat curved impeller. *Industrial Engineering Chemistry Research*. 43, 6534-6547.
- Lister, J.D., Smit, D.J. and Hounslow, M.J., 1995. Adjustable discretized population balance for growth and aggregation. *AIChE Journal*. 41, 591-603.
- Liu, H.Q. and Macedo, E.A., 1995. Accurate correlations for the selfdiffusion coefficients of CO<sub>2</sub>, CH<sub>4</sub>, C<sub>2</sub>H<sub>4</sub>, H<sub>2</sub>O, and D<sub>2</sub>O over wide ranges of temperature and pressure. *Journal of Supercritical Fluids*. 8, 310-317.
- Ma, C.Y., Tighe, C.J., Gruar, R.I., Mahmud, T., Darr, J.A. and Wang, X.Z., 2011. Numerical modelling of hydrothermal fluid flow and heat transfer in a tubular heat exchanger under near critical conditions. *Journal of Supercritical Fluids*. 57, 236-246.
- Ma, C.Y., Wang, X.Z., Tighe, C.J. and A., D.J., 2012. Modelling and simulation of counter-current and confined jet reactors for continuous hydrothermal flow synthesis of nano-materials. *IFAC-PapersOnLine - Advanced Control of Chemical Processes*, . 8, doi:10.3182/20120710-4-SG-2026.00073.
- Merkus, H.G. 2009. *Particle Size Measurements: Fundamentals, Practice, Quality*. Springer
- Middelkoop, V., Boldrin, P., Peel, M., Buslaps, T., Barnes, P., Darr, J.A. and Jacques, S.D.M., 2009. Imaging the inside of a Continuous Nanoceramic Synthesizer under Supercritical Water Conditions Using High-Energy Synchrotron X-Radiation. *Chemistry of Materials*. 21, 2430-2435.
- Moussiere, S., Jousset-Dubien, C., Guichardon, P., Boutin, O., Turc, H.-A., Roubaud, A. and Fournel, B., 2007. Modelling of heat transfer and hydrodynamic with two kinetics approaches during supercritical water oxidation process. *Journal of Supercritical Fluids*. 43, 324-332.
- Ohara, S., Mousavand, T., Umetsu, M., Takami, S., Adschiri, T., Kuroki, Y. and Takata, M., 2004. Hydrothermal synthesis of fine zinc oxide particles under supercritical conditions. *Solid State Ionics*. 172, 261-264.

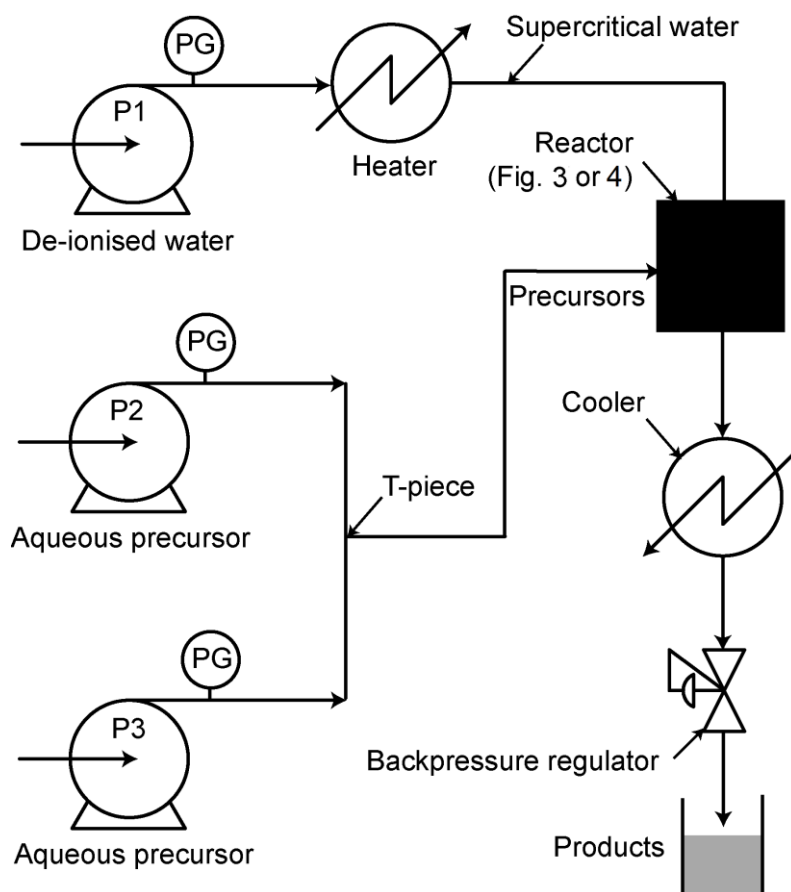
- Otsu, J. and Oshima, Y., 2005. New approaches of the preparation of metal oxide particles on the surface of porous materials using supercritical water: development of supercritical water impregnation. *Journal of Supercritical Fluids*. 33, 61-67.
- Paul, E.L., Atiemo-Obeng, V. and Kresta, S.M. 2003. *Handbook of Industrial Mixing: Science and Practice*. John Wiley & Sons
- Peukert, W., Schwarzer, H.C. and Stenger, F., 2005. Control of aggregation in production and handling of nanoparticles. *Chemical Engineering and Processing*. 44, 245-252.
- Sierra-Pallares, J., Alonso, E., Montequi, I. and Cocero, M.J., 2009. Particle diameter prediction in supercritical nanoparticle synthesis using three-dimensional CFD simulations. Validation for anatase titanium dioxide production. *Chemical Engineering Science*. 64, 3051-3059.
- Sierra-Pallares, J., Daniele L. Marchisio, D.L., Alonso, E., Parra-Santos, M.T., Castro, F. and Cocero, M.J., 2011. Quantification of mixing efficiency in turbulent supercritical water hydrothermal reactors *Chemical Engineering Science*. 66, 1576-1589.
- Smoluchowski, M.Z., 1917. Versuch Einer Mathematischen Theorie Der Koagulationskinetik Kolloider Losung. *Zeitschrift fur Physikalische Chemie*. 92, 129-142.
- Testino, A., Buscaglia, V., Buscaglia, M.T., Viviani, M. and Nanni, P., 2005. Kinetic modeling of aqueous and hydrothermal synthesis of barium titanate ( $\text{BaTiO}_3$ ). *Chemistry of Materials*. 17, 5346-5356.
- Tighe, C.J., Cabrera, R.Q. and Darr, J.A., 2013. Scale Up Production of Nanoparticles: Continuous Supercritical Water Synthesis of Ce-Zn Oxides *Industrial and Engineering Chemistry Research*. 52, 5522-5528
- Tighe, C.J., Gruar, R.I., Ma, C.Y., Mahmud, T., Wang, X.Z. and Darr, J.A., 2012. Mixing and heat transfer in continuous hydrothermal flow synthesis reactors; An in-situ investigation of counter-current mixing. *Journal of Supercritical Fluids*. 62, 165-172.
- Wagner, W. and Pruß, A., 2002. The IAPWS Formulation 1995 for the Thermodynamic Properties of Ordinary Water Substance for General and Scientific Use. *Journal of Physical and Chemical Reference Data*. 31, 387-535.
- Woo, X.Y., Tan, R.B.H. and Braatz, R.D., 2009. Modeling and computational fluid dynamics-population balance equation-micromixing simulation of impinging jet crystallizers. *Crystal Growth and Design*. 9, 154-164.
- Woo, X.Y., Tan, R.B.H., Chow, P.S. and Braatz, R.D., 2006. Simulation of mixing effects in antisolvent crystallization using a coupled CFD-PDF-PBE approach. *Crystal Growth & Design*. 6, 1291-1303.
- Yang, W.C. 2003. *Handbook of Fluidization and Fluid-particle Systems: Texte Imprimé*. Marcel Dekker
- Zhang, Q., Yong, Y., Mao, Z.-S., Yang, C. and Zhao, C., 2009. Experimental determination and numerical simulation of mixing time in a gas-liquid stirred tank. *Chemical Engineering Science*. 64, 2926-2933.

**Table 1.** Operating conditions for experiments and simulations (operating pressures of supercritical water (ScH<sub>2</sub>O) and precursor streams fixed at 24.1 MPa)

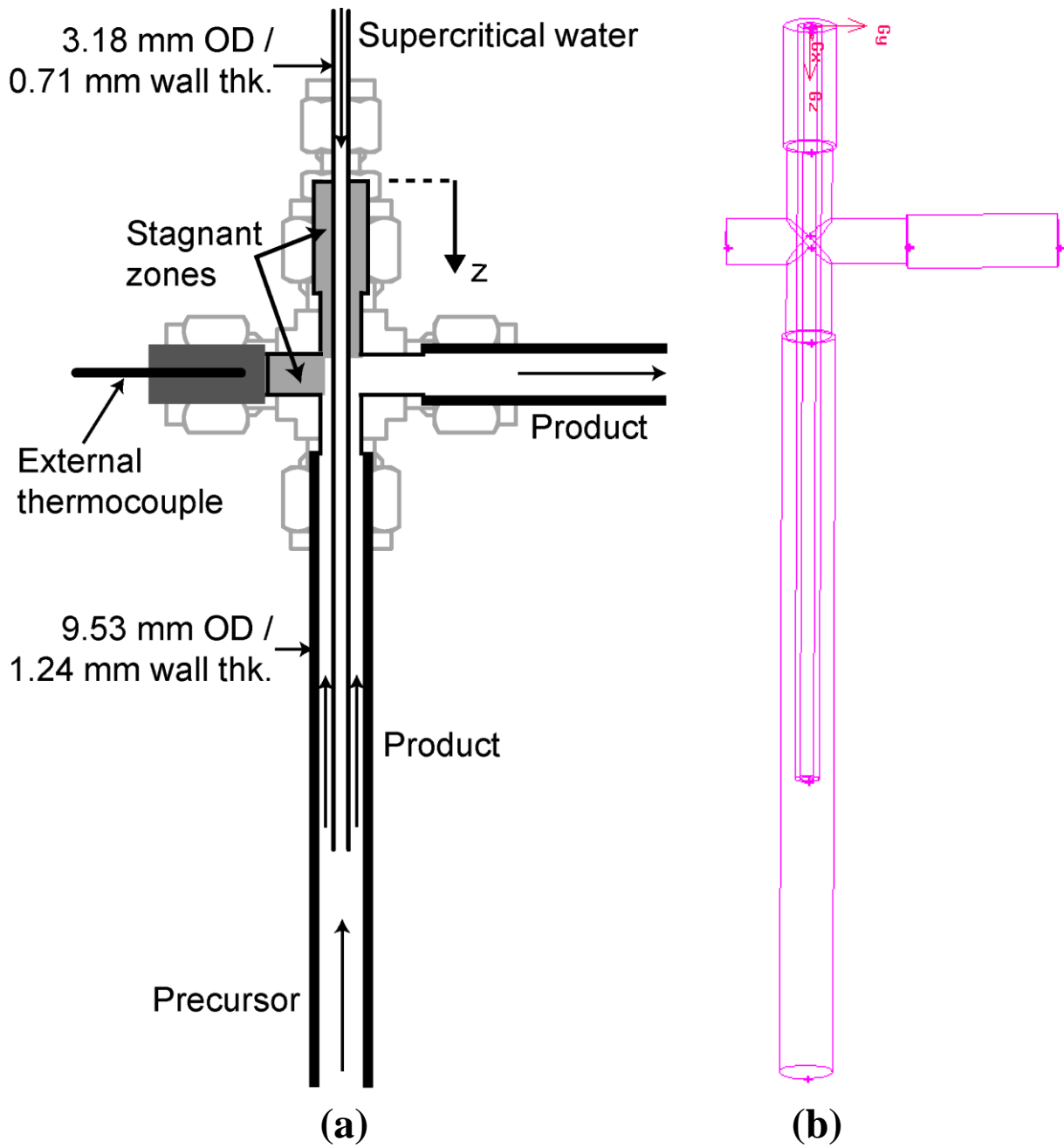
Reactor type	precursor		ScH <sub>2</sub> O		tracer		ScH <sub>2</sub> O with tracer	
	flowrate (mL/min)	temperature T <sub>in</sub> (°C)	flowrate (mL/min)	T <sub>in</sub> (°C)	flowrate (mL/min)	T <sub>in</sub> (°C)	flowrate (mL/min)	T <sub>in</sub> (°C)
Counter-current	20	20	20	400	0.2	400	19.8	400
Confined jet	20	20	20	400	0.2	400	19.8	400



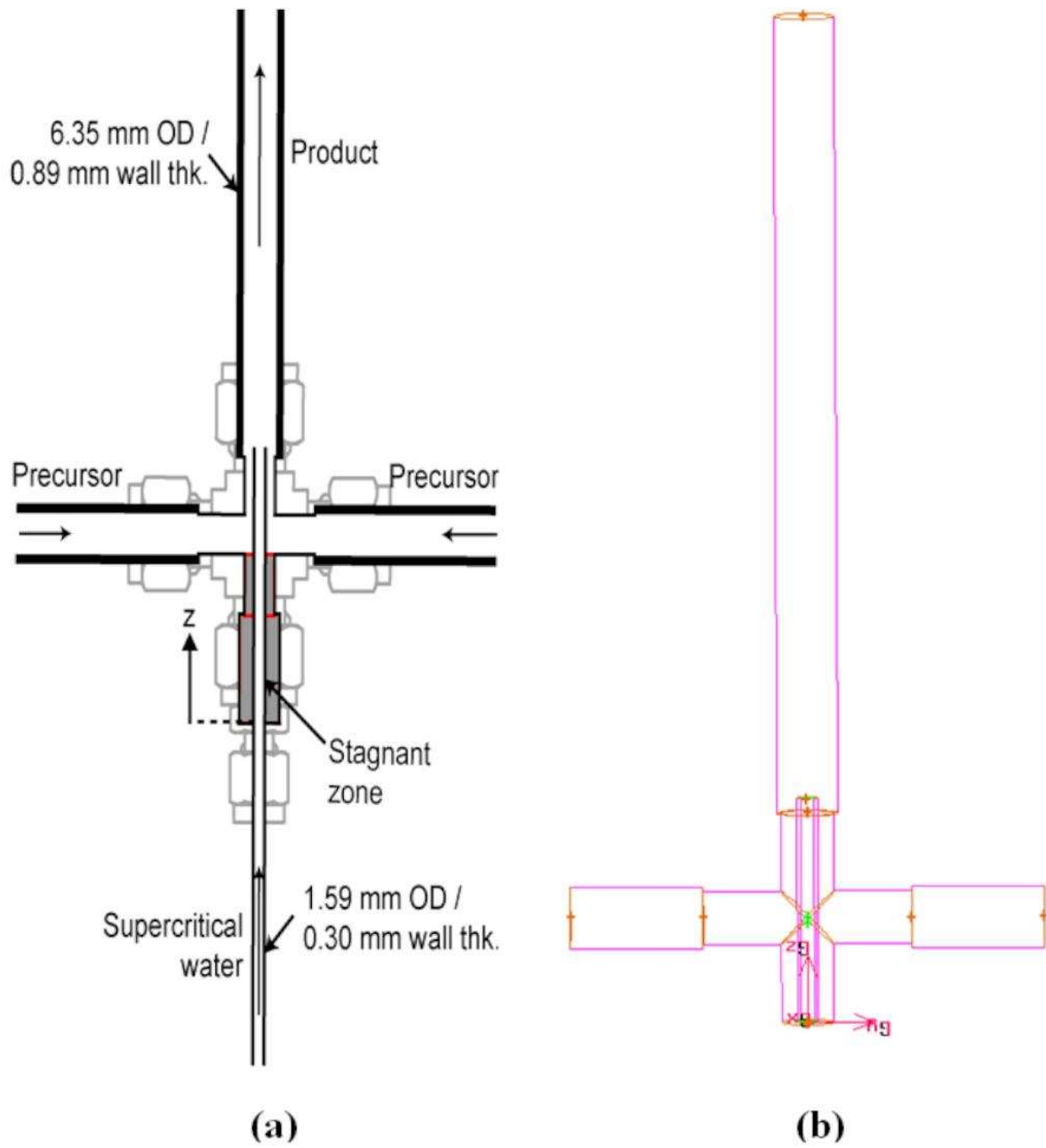
**Figure 1.** Thermodynamic properties of supercritical water under a constant pressure of 24.1 MPa (Ma et al., 2011) (Red solid line – density ( $\rho$ ; kg/m<sup>3</sup>); Blue dotted line – specific heat ( $C_p/90$ ; J/(kg K)); Green dashed line with dots – thermal conductivity ( $\kappa \times 2000$ ; W/(m K)); Black dashed line – viscosity ( $\mu \times 10^5$ ; Pa s)).



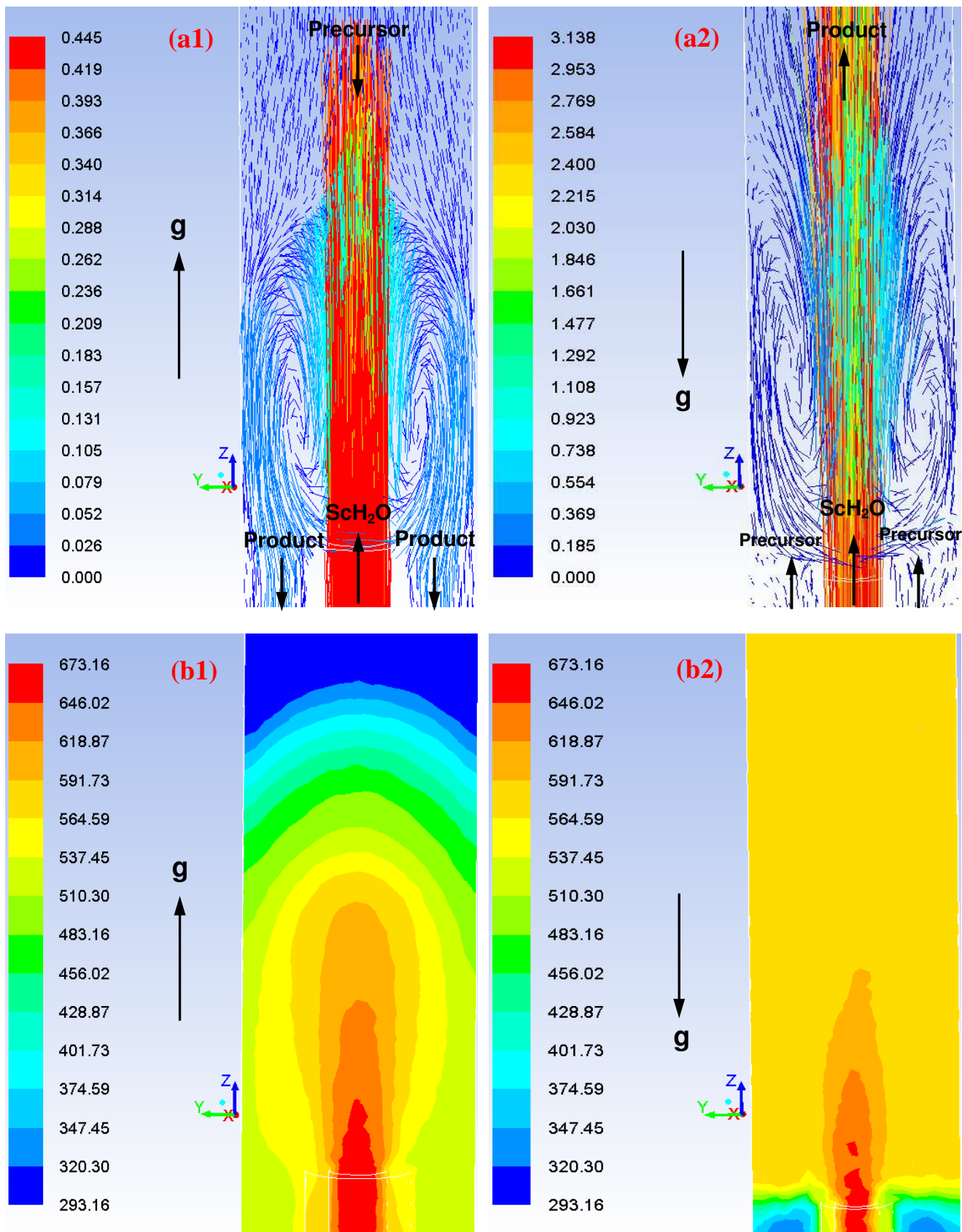
**Figure 2.** Flow diagrams of a CHFS system with a counter-current reactor or a confined jet mixer.



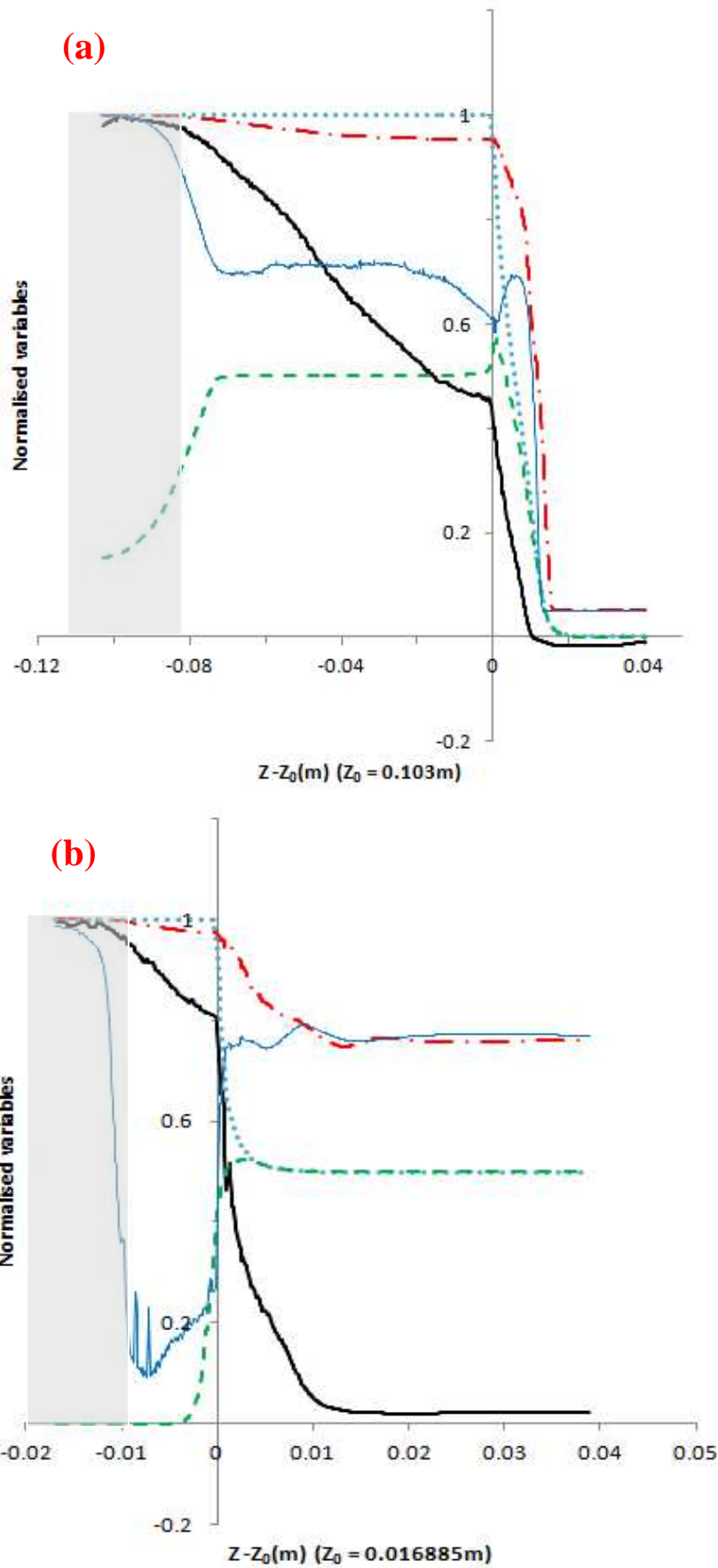
**Figure 3.** (a) schematic diagrams of a counter-current reactor with dimensions and the positions of the thermocouples used in experiments, (b) computational domain.



**Figure 4.** (a) schematic diagrams of a confined jet mixer used in experiments, (b) computational domain.

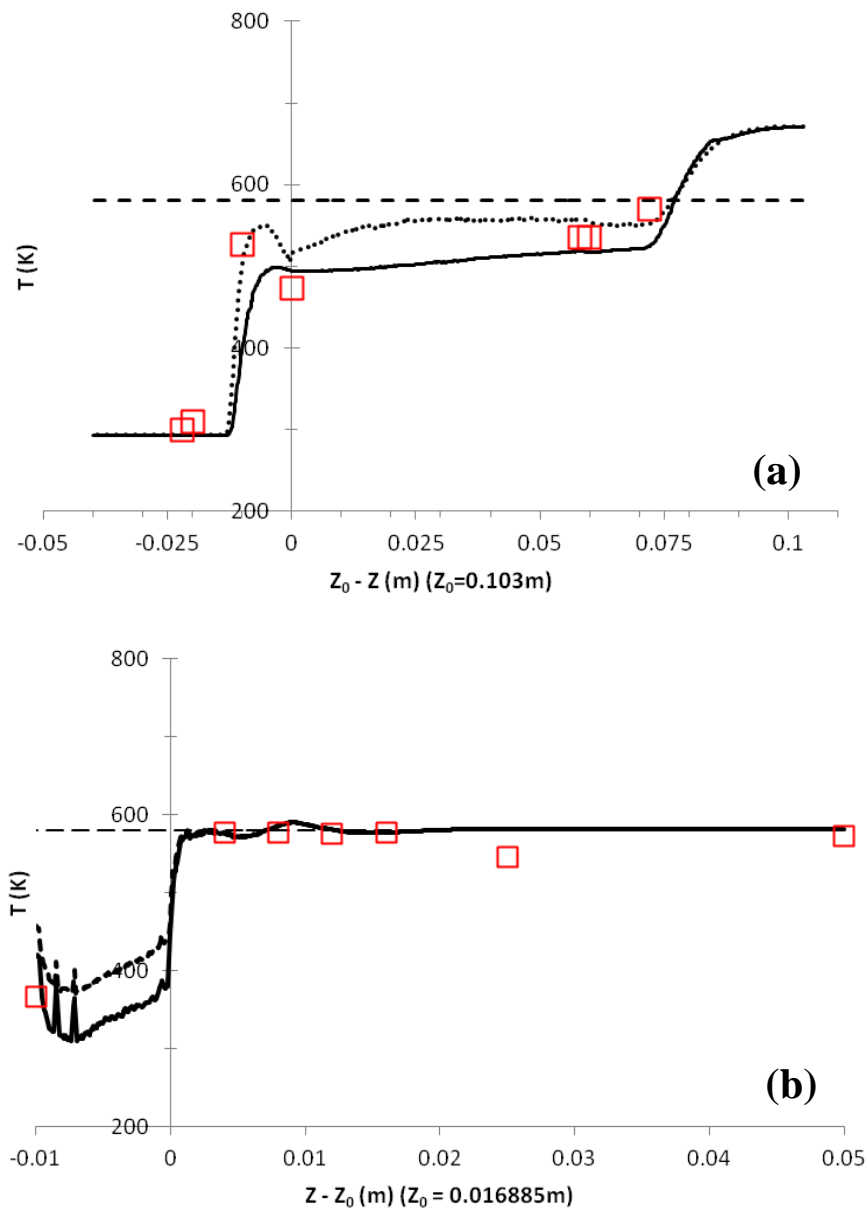


**Figure 5.** Velocity vectors (a1, a2) and temperature (b1, b2) distributions in the supercritical water (ScH<sub>2</sub>O) exit regions of a counter-current reactor (a1, b1) and a confined jet mixer (a2, b2). Note that for comparison purpose, Figure 5(a1, b1) were plotted with a rotation of 180°.

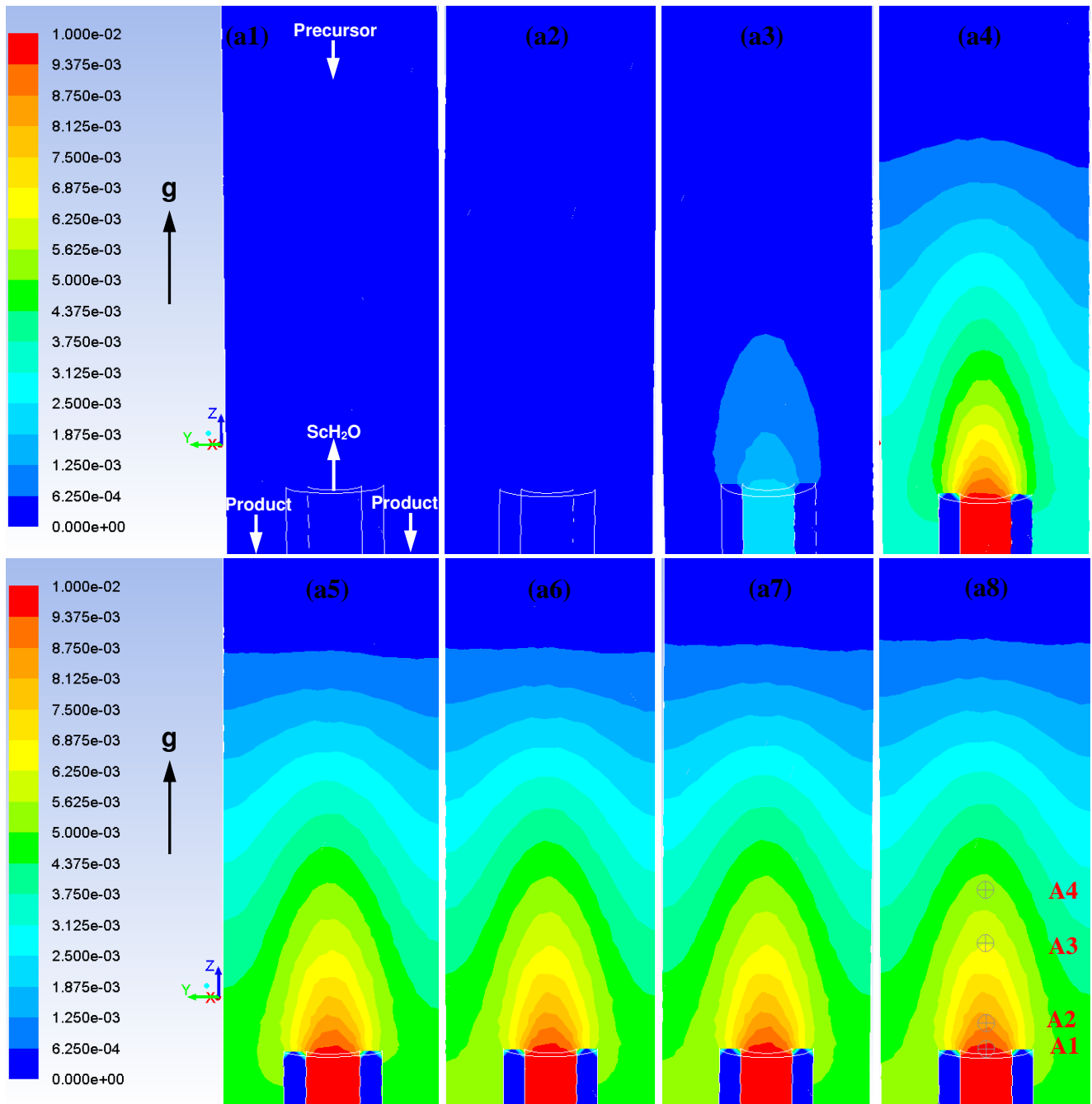


**Figure 6.** (a) Axial velocity (solid line), temperature (dash and dot line) and tracer concentration (dotted line) along the centreline ( $x = 0, y = 0$ ), and temperature (thin solid line) and tracer concentration (dashed line) along a line ( $x = 0, y = 1.7\text{ mm}$ ) in the  $z$  direction for a counter-current

reactor; (b) Axial velocity (solid line), temperature (dash and dot line) and tracer concentration (dotted line) along the centreline ( $x = 0, y = 0$ ), and temperature (thin solid line) and tracer concentration (dashed line) along a line ( $x = 0, y = 1 \text{ mm}$ ) in the  $z$  direction for a confined jet mixer. The values of the variables were normalised by their corresponding inlet values. The shadow areas are in the stagnant regions near the inlet of the supercritical water streams.



**Figure 7.** Predicted and measured (red squares) temperature distributions along the  $z$  direction (a) counter-current reactor (dotted line –  $y = 1.7$  mm; solid line –  $y = 2.9$  mm); (b) confined jet mixer (solid line –  $y = 1.2$  mm; dashed line –  $y = 1.0$  mm).



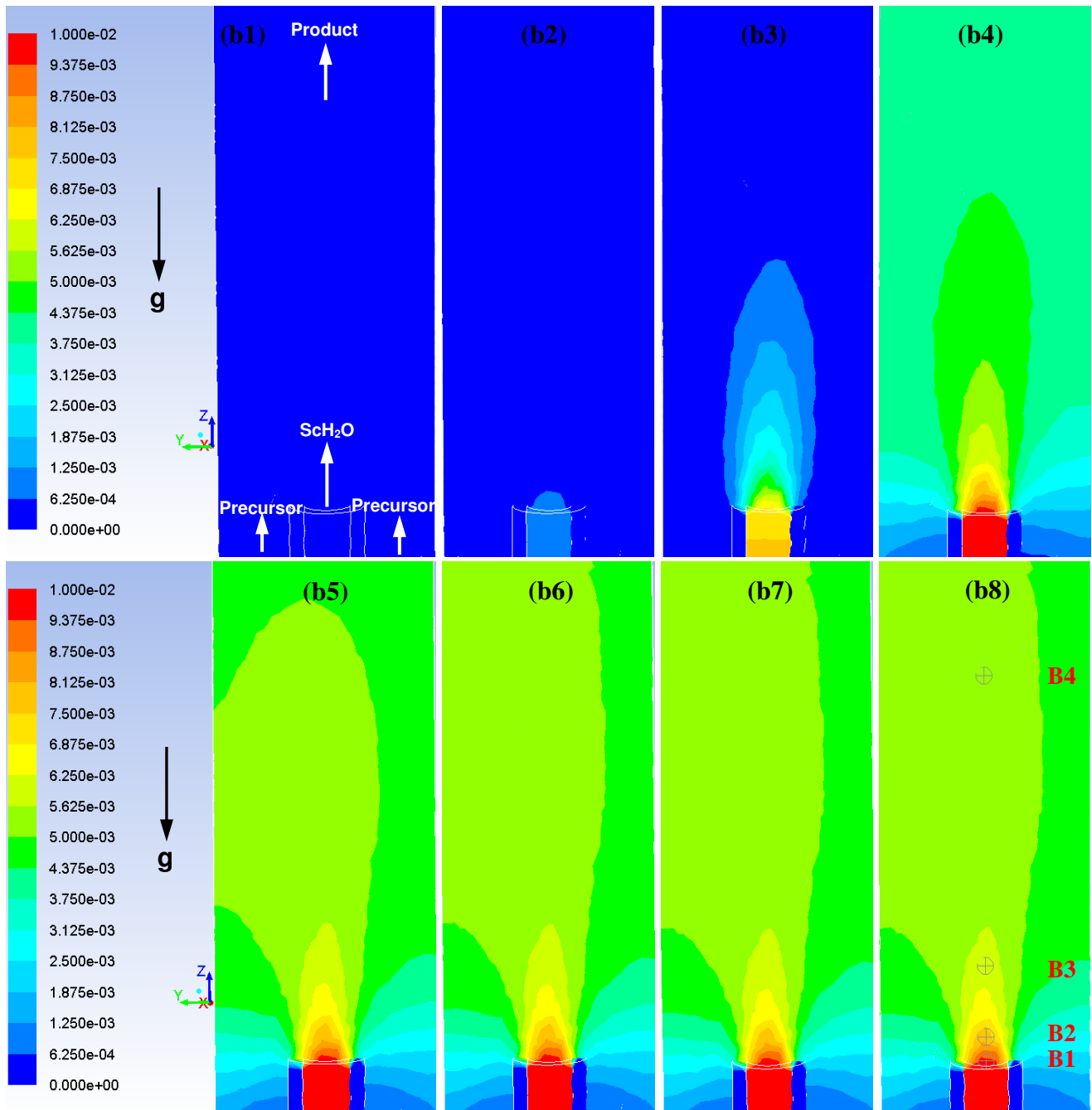


**Figure 8.** Contours of tracer concentrations in mass fraction in a counter-current reactor at 0.01 s (a1), 0.3 s (a2), 0.5 s (a3), 1.5 s (a4), 3.5 s (a5), 7.5 s (a6), 9.0 s (a7) and 15.0 s (a8) with four monitoring points, A1, A2, A3 and A4 ( $\Delta L/D_i = 0, 0.5, 2$  and  $3$ ); and in a confined jet mixer at 0.01 s (b1), 0.02 s (b2), 0.05 s (b3), 0.5 s (b4), 1.5 s (b5), 3.0 s (b6), 5.0 s (b7) and 15.0 s (b8) with four monitoring points, B1, B2, B3 and B4 ( $\Delta L/D_i = 0, 0.5, 2$  and  $8$ ). Note that for comparison purpose, Figure 8(a1 – a8) was plotted with a rotation of  $180^\circ$ .

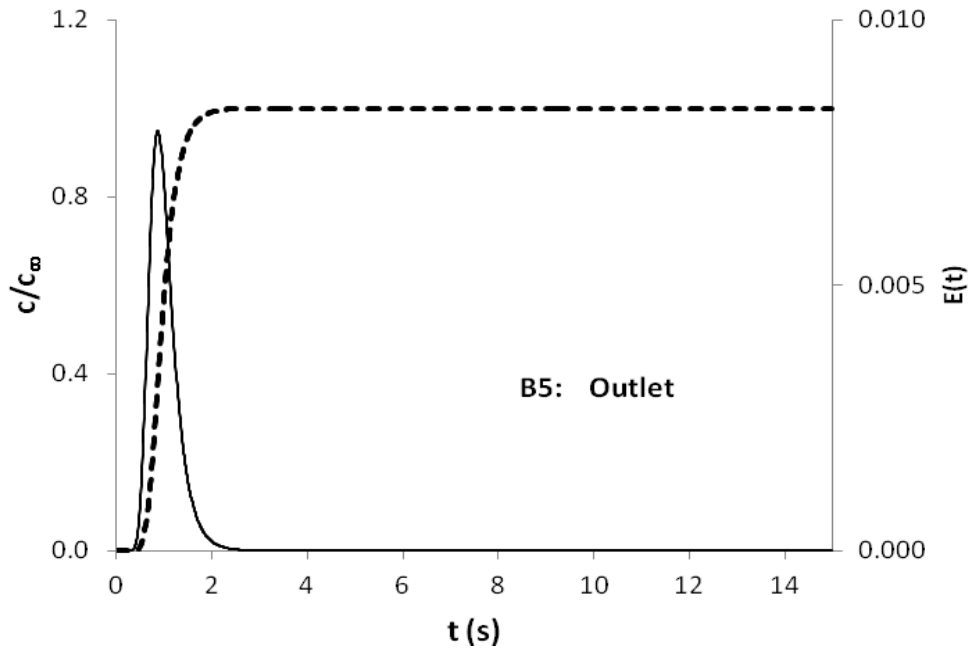
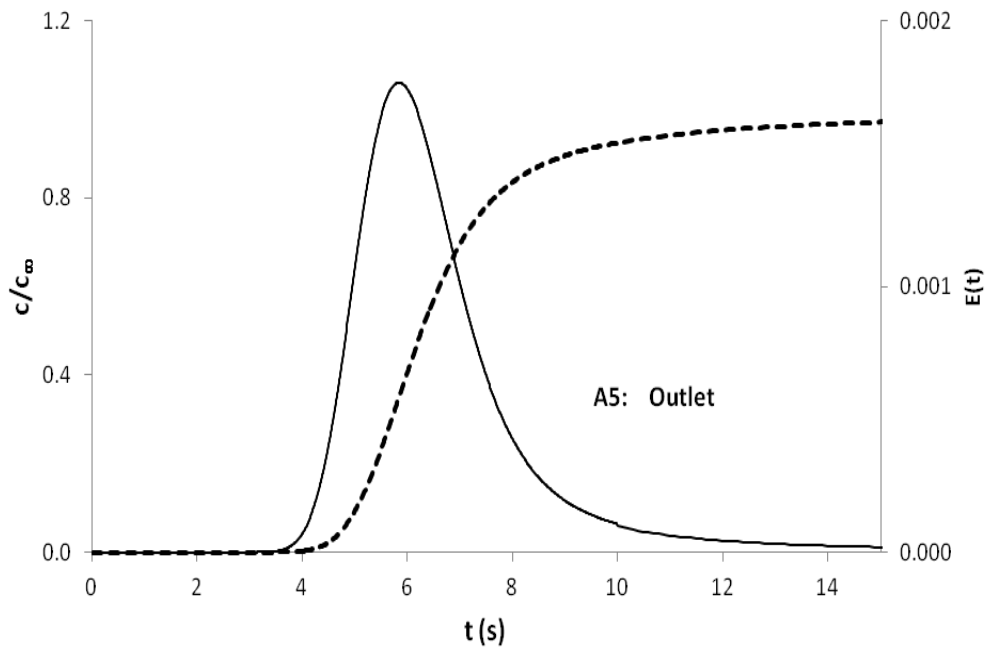


**Figure 9.** Tracer mass fraction variations –  $c/c_{\infty}$  (dashed lines) and residence time distributions –  $E(t)$  (solid lines) vs. time at the reactor outlet (A5) counter-current reactor; (B5) confined jet mixer.

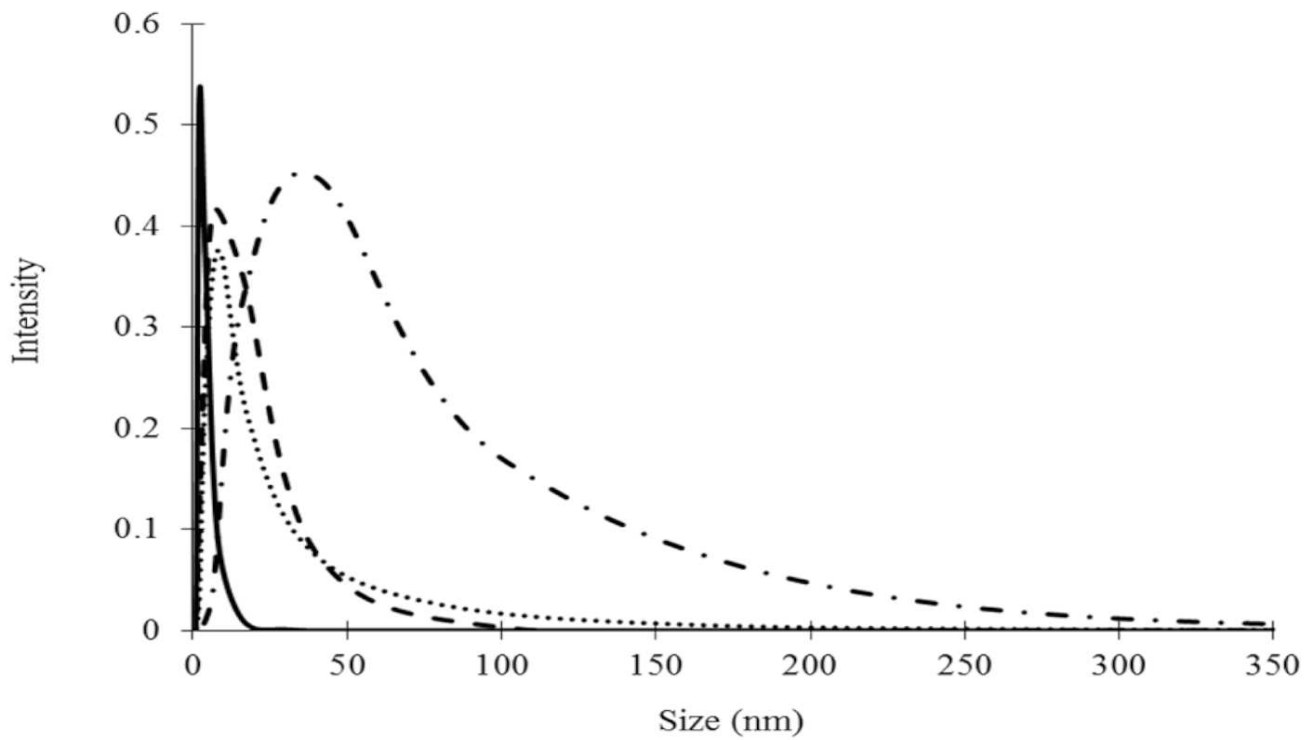


**Figure 10.** Comparison of PSDs presented as number intensity ( $N_i/N$ ) vs.  $D_i$  (solid line – confined jet mixer without aggregation; dot line – confined jet mixer with aggregation; dash line – counter current reactor without aggregation; dot and dash line – counter current reactor with aggregation).